Fundamental Research 3 (2023) 822–830

Contents lists available at ScienceDirect

Fundamental Research

journal homepage: http://www.keaipublishing.com/en/journals/fundamental-research/

Article

High-Q collective Mie resonances in monocrystalline silicon nanoantenna arrays for the visible light

Zhenghe Zhang[a,b,1], Pengbo Liu[a,b,1], Wanli Lu[c], Ping Bai[d], Bingchang Zhang[a,b], Zefeng Chen[a,b], Stefan A. Maier[e,f,g], Jaime Gómez Rivas[d], Shaojun Wang[a,b,*], Xiaofeng Li[a,b,*]

[a] School of Optoelectronic Science and Engineering & Collaborative Innovation Center of Suzhou Nano Science and Technology, Soochow University, Suzhou 215006, China
[b] Key Lab of Advanced Optical Manufacturing Technologies of Jiangsu Province & Key Lab of Modern Optical Technologies of Education Ministry of China, Soochow University, Suzhou 215006, China
[c] School of Materials Science and Physics, China University of Mining and Technology, Xuzhou 221116, China
[d] Department of Applied Physics and Institute for Photonic Integration, Eindhoven University of Technology, 5612 AE Eindhoven, The Netherlands
[e] School of Physics and Astronomy, Monash University, Clayton, Victoria 3800, Australia
[f] Department of Physics, Imperial College London, London SW7 2AZ, UK
[g] Chair in Hybrid Nanosystems, Nanointitute Munich, Faculty of Physics, Ludwig-Maximilians Universitaet Muenchen, Muenchen 80539, Germany

ARTICLE INFO

Article history:
Received 1 December 2021
Received in revised form 6 May 2022
Accepted 10 May 2022
Available online 11 June 2022

Keywords:
Nanophotonics
Dielectric resonators
Surface lattice resonances
Bound states in the continuum
Quasi-guided modes

ABSTRACT

Dielectric optical antennas have emerged as a promising nanophotonic architecture for manipulating the propagation and localization of light. However, the optically induced Mie resonances in an isolated nanoantenna are normally with broad spectra and poor *Q*-factors, limiting their performances in sensing, lasing, and nonlinear optics. Here, we dramatically enhance the *Q*-factors of Mie resonances in silicon (Si) nanoparticles across the optical band by arranging the nanoparticles in a periodic lattice. We select monocrystalline Si with negligible material losses and develop a unique method to fabricate nanoparticle arrays on a quartz substrate. By extinction dispersion measurements and electromagnetic analysis, we can identify three types of collective Mie resonances with *Q*-factors ~ 500 in the same nanocylinder arrays, including surface lattice resonances, bound states in the continuum, and quasi-guided modes. Our work paves the way for fundamental research in strong light-matter interactions and the design of highly efficient light-emitting metasurfaces.

1. Introduction

Optical antennas, analogies to microwave or radiowave antennas, can convert the freely propagating light field into localized energy, and vice versa [1]. These artificial subwavelength architectures (also called meta-atoms) offer us a desirable platform for pursuing the fundamental insights into the control and manipulation of light or matter [2,3]. It enables a variety of possibilities to develop relevant applications in photodetection [4,5], solid-state lighting [6,7], lasing [8–10], bio-sensing [11,12], and quantum technologies [3,13,14]. Over the past decades, plasmonic antennas composed of metallic nanoparticles have achieved the deep-subwavelength-scale optical localization for the highly efficient manipulation of light [15,16]. Intrinsic to metals are Ohmic losses and skin effect due to the free electrons in conductors. The plasmonic nanoparticles thus possess essentially high material losses and can not support magnetic resonances inside without any exceptional design as well [17,18].

Recently, optically induced dielectric resonators have emerged as a vibrant scheme to proceed the development of nanophotonics [9,10,18–27]. The high-index dielectric nanoparticles are of negligible absorption losses. They can simultaneously support electric and magnetic Mie resonances due to the optically induced displacement currents, leading to high local field enhancements. Additionally, the interference of coupling between different multipole resonances in dielectric nanoparticles can lead to a plethora of new phenomena, including nonradiating anapole modes [23], Kerker effects [19,27], and accidental bound states in the continuum (BICs) [28,29].

Among different types of dielectrics and semiconductors, silicon (Si) is the most plausible material to design optical nanoantennas considering its high refractive index, low losses, and CMOS-compatible fabrication processes [18,26,30,31]. Under the illumination of light, an isolated

* Corresponding authors.
E-mail addresses: swang.opto@suda.edu.cn (S. Wang), xfli@suda.edu.cn (X. Li).
[1] These authors contributed equally to this work.

https://doi.org/10.1016/j.fmre.2022.05.020

Si nanoparticle has a large scattering cross-section due to its strong optically induced polarizability. The nanoparticle radiates efficiently to free space while resulting in a broad spectrum and poor quality (Q)-factor. To suppress the radiation losses of the isolated nanoparticles, nonradiating configurations confining anapole and BIC resonances have been employed to enhance the field confinement inside the particle [23,28,29]. While real applications typically require field enhancements specifically extending to the surrounding of the nanoparticles. In contrast, the collective Mie resonances in nanoparticle arrays (NPAs) arranged in a periodic lattice can dramatically boost the field enhancement over large volumes, and thus the light-matter interaction involving a high density of quantum emitters in the proximity of the nanoparticles. Additionally, current Si NPAs are mostly fabricated using amorphous Si (a-Si) [12,19,32,33], which has an absorption coefficient as one order of magnitude larger than monocrystalline Si (c-Si) [34]. The efforts to prepare c-Si NPAs on a desirable substrate have been strongly hampered by the fabrication complexity [20,35–37].

In this article, we simplify the fabrication processes of c-Si NPAs and successfully achieve three types of collective Mie resonances with ultra-low losses in the visible. We prepare c-Si NPAs on a transparent substrate with a low refractive index (e.g. quartz) employing a "float off" technique, inspired by the wet transfer of two-dimensional materials [38]. We resolve different multipole resonances in c-Si NPAs from their extinction spectra and near-field simulations by tuning the period of the lattice and diameter of the nanoparticles. We demonstrate sharp magnetic surface lattice resonances (SLRs) with Q-factors as high as ~ 500 at wavelengths longer than 600 nm, thanks to the negligible absorption coefficients of c-Si in this band and in-phase scattering assisted by the lattice. Furthermore, we observe a symmetry-protected BIC mode without radiation in the normal direction, showing a readable Q-factor of ~ 180 close to the Γ point of the lattice when the symmetry is broken. From the electromagnetic analysis of multipole decomposition, we identify that the BIC mode with lower energy than that of the diffraction order of the lattice arises from the out-of-plane magnetic dipolar resonances inside the NPAs, while a quasi-BIC mode with energy close to the diffraction order is contributed by the in-plane electric quadrupoles. Furthermore, we hybridize the Mie resonances with guided modes, spatially extending the optical field to a lossless slab, and obtain modest high-Q quasi-guided modes (QGMs) at the optical band lower than 550 nm. Our work suggests that the fine engineering of all-dielectric nanoantenna arrays provides a myriad of possibilities to achieve super long-lived optical resonances. It can not only proceed the fundamental study of strong light-matter interactions, but also intrigue the applications of antenna metasurfaces in display [31,39], optoelectronic detection [40], and visible light communications [41].

2. Material and methods

2.1. Sample fabrication

The c-Si NPA on a SOI wafer (ShinEtsu Inc.) was fabricated using electron beam lithography (EBL) and dry etching in advance (Fig. S1). The wafer includes a 100 nm thick intrinsic c-Si layer and a 450 nm thick SiO_2 layer. A hole array pattern was firstly formed on positive resist (PMMA A2, MicroChem) with a thickness of 80 nm using an EBL (JBX-5500FS, JEOL) with a dose of 450 μC/cm^2 and a beam current of 2 nA. Afterward, a 4 nm thick alumina was deposited onto the hole array pattern of resist by atomic layer deposition. A nanodisk array pattern of alumina was formed when the resist was removed with anisole in an ultrasonic cleaner followed by an oxygen plasma cleaner. The alumina disk array pattern then was transferred to the 100 nm SOI device layer using a Bosch process with SF_6 and C_4H_8 [42,43]. The etching rate of c-Si was tuned to 0.5 nm/s to avoid etching the oxide layer of SOI as much as possible. Afterward, a PMMA layer with a thickness of 300-600 nm was spin-cast onto the c-Si NPAs.

The whole sample was immersed in hydrofluoric (HF) acid with a concentration of 40% for 24 hours to etch the 450 nm thick SiO_2 layer between c-Si NPAs and the silicon substrate. Then the sample was moved to the deionized water. The PMMA slab embedding the c-Si NPAs floated off and was titled onto another silicon wafer. Such “float off” was repeated in different bottles of deionized water for three times to clean the residuals of HF. The PMMA slab was finally loaded onto a quartz substrate in deionized water. In this process, the PMMA slab also can be subtly turned over to prepare a c-Si NPAs facing the air after being transferred onto a quartz substrate [44]. The surface morphology of c-Si NPA embedded in PMMA was scanned by an atomic force microscope (Fig. S2). The sample can be covered on a flexible PDMS superstrate with a thickness of 200 μm for ensuring a dielectric environment for c-Si NPAs with a nearly homogeneous refractive index.

2.2. Optical characterization

The refractive index of the c-Si layer on SOI was measured using ellipsometry (GES5E, SEMLAB). The extinction spectra at normal incidence of the c-Si NPAs were measured using an optical microscope. The sample was aligned along the optical axis of the microscope and illuminated with quasi-collimated white light from a halogen tungsten lamp. The light transmitted through the samples was collected using a microscope objective (CFI Plan Fluor 4x, NA = 0.13, Nikon) and recorded with an imaging spectrometer (Shemrock 500i) with a grating of 150 lines/mm at 500 nm blaze wavelength and an electron-multiplying charge-coupled device camera (EMCCD, iXon Ultra 888).

The extinction dispersion measurements were carried out with a home-built Fourier imaging setup (Fig. S5a). It consists of an inverted microscope (Nikon Ti2-U) equipped with a couple of objectives with the same optical parameters (Plan Fluor ELWD 60x, NA = 0.7, Nikon). The quasi-collimated incident light is focused onto the sample through the former objective and the transmitted light from the sample passes through the latter objective. A Fourier lens (FL) at the side port of the microscope copies the back focal plane image (i.e. Fourier image) of the latter objective to infinity. Another tube lens (TL) focuses the Fourier image onto the slit of the spectrometer coupled with EMCCD. A linear polarizer between the FL and TL defines the polarization of the beam [43–45].

2.3. Numerical simulations

The extinction and near-field simulations were performed using the finite-difference time-domain method (FDTD) with the commercial package Lumerical. The sharp corners of cylinders were replaced by sphere sections with a radius of 10 nm to avoid extreme hot spots and to approach the experimental conditions. Non-dispersive refractive indices for quartz, PDMS superstrate, PMMA layer, and alumina residuals were employed. The optical constants of c-Si were obtained from the ellipsometry measurement. For the simulations of the scattering cross-section and the Cartesian distribution of the near-field, a total-filed scattered-field (TFSF) source and perfectly matched layer (PML) boundaries were implemented. While in-plane wave sources, periodic boundary conditions in the in-plane directions (x- or y-axis), and PML boundaries in the out-of-plane direction (z-axis) were used for the arrays.

We further use the multipole decomposition approach to fully identify the Cartesian components of multipoles excited inside the nanoparticles [46–48]. Briefly, we record the field amplitude ($\boldsymbol{E}$) inside of the particle for a unit cell under the excitation of in-plane waves as a function of the incident angles. We use for these simulations the finite-element method, instead of FDTD, because of the accessible integral calculations in COMSOL. We can obtain the polarization currents ($\boldsymbol{j}$) induced inside the nanoparticles using the equation:

$$\boldsymbol{j} = -i\omega\varepsilon_0(\varepsilon - \varepsilon_d)\boldsymbol{E}, \quad (1)$$

where ω is the frequency of the multipole resonance, and ε_0, ε, and ε_d are the permittivity of free space, Si, and PMMA, respectively. Based on the distribution of polarization current inside the nanoparticle, we further calculate the electric, magnetic, and toroidal dipole moments:

$$p_\alpha = \frac{i}{\omega}\int_V j_\alpha d^3r, \tag{2}$$

$$m_\alpha = \frac{1}{2}\int_V (\boldsymbol{r}\times\boldsymbol{j})_\alpha d^3r, \tag{3}$$

$$T_\alpha = \frac{1}{10}\int_V \left[(\boldsymbol{j}\cdot\boldsymbol{r})r_\alpha - 2r^2 j_\alpha\right]d^3r, \tag{4}$$

where $\boldsymbol{r}$ defines the spatial position in Cartesian coordinates, and α (β below as well) thus refers to x, y, z. Next we obtain the quadrupolar moments [48]:

$$Q^e_{\alpha\beta} = \frac{i}{\omega}\int_V \left[r_\alpha j_\beta + r_\beta j_\alpha - \frac{2}{3}\delta_{\alpha\beta}(\boldsymbol{r}\times\boldsymbol{j})\right]d^3r, \tag{5}$$

$$Q^m_{\alpha\beta} = \frac{1}{3}\int_V \left[(\boldsymbol{r}\times\boldsymbol{j})_\alpha r_\beta + (\boldsymbol{r}\times\boldsymbol{j})_\beta r_\alpha\right]d^3r, \tag{6}$$

$$Q^T_{\alpha\beta} = \frac{1}{42}\int_V \left[4(\boldsymbol{r}\cdot\boldsymbol{j})r_\alpha r_\beta + 2(\boldsymbol{j}\cdot\boldsymbol{r})r^2\delta_{\alpha\beta} - 5r^2\left(r_\alpha j_\beta + r_\beta j_\alpha\right)\right]d^3r, \tag{7}$$

and the mean-square radii of the dipole or quadrupole distributions are given by:

$$M^{\langle 2\rangle}_\alpha = \frac{i\omega}{20}\int_V r^2(\boldsymbol{r}\times\boldsymbol{j})_\alpha d^3r, \tag{8}$$

$$T^{\langle 2\rangle}_\alpha = \frac{1}{280}\int_V \left[3r^4 j_\alpha - 2r^2(\boldsymbol{r}\cdot\boldsymbol{j})r_\alpha\right]d^3r, \tag{9}$$

$$Q^{m\langle 2\rangle}_{\alpha\beta} = \frac{i\omega}{42}\int_V r^2\left[(\boldsymbol{r}\times\boldsymbol{j})_\alpha r_\beta + (\boldsymbol{r}\times\boldsymbol{j})_\beta r_\alpha\right]d^3r. \tag{10}$$

Finally, we get the scattering cross-sections of electric/magnetic dipolar and quadrupolar resonances of the lattice in SI units using:

$$C^{\mathrm{ED}}_{\mathrm{sca}} = \frac{k_0^4}{6\pi\varepsilon_0^2 E_0^2}\sum_\alpha \left|p_\alpha + \frac{ik_0\varepsilon_d}{c}T_\alpha + \frac{ik_0^3\varepsilon_d^2}{c}T^{\langle 2\rangle}_\alpha\right|^2, \tag{11}$$

$$C^{\mathrm{MD}}_{\mathrm{sca}} = \frac{\eta_0^2 k_0^4\varepsilon_d}{6\pi E_0^2}\sum_\alpha \left|m_\alpha + \frac{ik_0\varepsilon_d}{c}M^{\langle 2\rangle}_\alpha\right|^2, \tag{12}$$

$$C^{\mathrm{EQ}}_{\mathrm{sca}} = \frac{k_0^6\varepsilon_d}{80\pi\varepsilon_0^2 E_0^2}\sum_{\alpha\beta} \left|Q^e_{\alpha\beta} + \frac{ik_0\varepsilon_d}{c}Q^T_{\alpha\beta}\right|^2, \tag{13}$$

$$C^{\mathrm{MQ}}_{\mathrm{sca}} = \frac{\eta_0^2 k_0^6\varepsilon_d^2}{80\pi E_0^2}\sum_{\alpha\beta} \left|Q^m_{\alpha\beta} + \frac{ik_0\varepsilon_d}{c}Q^{m\langle 2\rangle}_{\alpha\beta}\right|^2, \tag{14}$$

where E_0 is the electric field amplitude of the incident waves, k_0 is its wave-vector, and η_0 is the impedance of free space.

3. Results and discussion

3.1. Mechanism for enhancing the Q-factors

The Q-factor of resonators is inversely proportional to their losses, including both the radiation loss and the constituent material loss due to absorption. To reduce the radiation loss, we arrange the Si nanoparticles in a square lattice (Fig. 1c) and investigate the collective Mie resonances (panels a and b of Fig. 1) inherent to the diffraction array or subdiffraction metasurface. Specifically, the NPAs are surrounded by dielectrics with a homogeneous refractive index or embedded in a polymer slab with a refractive index higher than that of the substrate. The enhanced radiative coupling between the individual nanoparticles for these two structures is through the diffraction orders in the plane of the array (i.e., Rayleigh anomalies or RAs) and planar waveguided modes, respectively

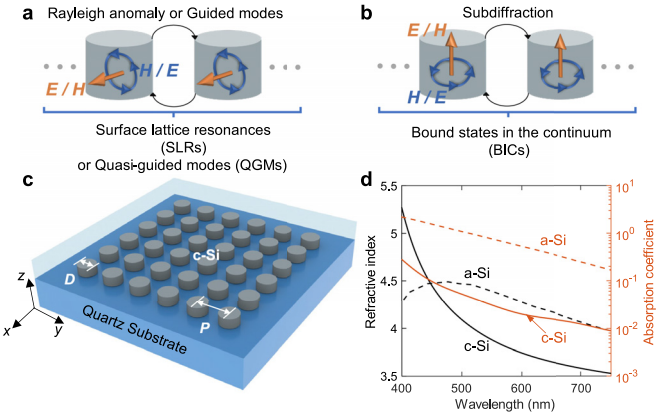

Fig. 1. Enhancing the quality (Q) factors of nanoantenna resonators by reducing their radiation losses and constituent material absorption. (a) Periodic arrays of dielectric nanoparticles support collective Mie resonances, emerging from the enhanced radiative coupling of localized electric or magnetic multipoles by in-plane diffraction orders, i.e., Rayleigh anomalies (RA) or guided modes. The former behaves as the so-called surface lattice resonances (SLRs), while the latter is the quasi-guided modes (QGMs). SLRs and QGMs can have remarkably narrow linewidths (high Q-fators) due to low radiation losses. **(b)** The coupling of out-of-plane dipoles or quadrupoles in a subdiffraction array with a C_4 symmetry manifests the third type of collective Mie resonances, i.e., symmetry-protected bound states in the continuum (BICs). The radiation channels of such BICs can be fully suppressed, offering a unique optical resonance with an infinite large Q-factor if the constituent material's absorption is negligible and the size of the array is ideally infinite. **(c)** Schematic of the sample. The monocrystalline silicon (c-Si) nanoparticle array (NPAs) on a quartz substrate (n = 1.45) consists of cylinders with varied diameters of D and a fixed height of 100 nm, and a square lattice with a period of P. The nanoparticles are coated with a slab of PMMA polymer (n = 1.49). The array is in the xy-plane, while the out-of-plane direction is indicated by the z-axis. **(d)** Comparisons of the refractive indices and absorption coefficients between c-Si and amorphous silicon (a-Si) in the visible band (λ = 400 - 750 nm). The black and orange curves represent the refractive indices and absorption coefficients, respectively. The solid and dashed curves correspond to the dispersion of c-Si and a-Si, respectively.

[2,5,6,49–52]. The hybridization of Mie resonances with surface propagating modes in terms of RAs and planar guided modes results in SLRs and QGMs, respectively (Fig. 1a) [53]. Such hybrid modes essentially suppress most of the radiation channels of the electric or magnetic multipoles within the individual nanoparticle. Therefore, SLRs and QGMs can improve the Q-factors of the isolated resonators by orders of magnitude [2].

To further inhibit the radiation losses of nanoantennas, we apply symmetry-protected BIC modes within a subdiffraction metasurface (Fig. 1b). Such BIC emerges from out-of-plane Mie dipolar or quadrupolar resonances which have no radiation channel to the normal direction of the C_4-symmetric array [8,9,26]. The BIC eigenmodes in an infinite NPA exhibit a characteristic suppression of the radiation, for which the electromagnetic field is confined on the plane of the array while completely decoupled from the radiation field in the free space. It provides a physical mechanism for trapping electromagnetic fields in small mode volumes for a long time [54]. In addition to engineering the radiation channels, we employ c-Si instead of a-Si, with a similar refractive index but a much lower absorption coefficient (Fig. 1c). A large index of c-Si allows the strong localization of electromagnetic field according to the small mode volume of the nanoantennas. A negligible absorption coefficient of c-Si not only displays the crucial advantages to the plasmonic counterparts but also allows to observe magnetic multipoles due to the electric loop inside the nanoparticles with high visibility [42].

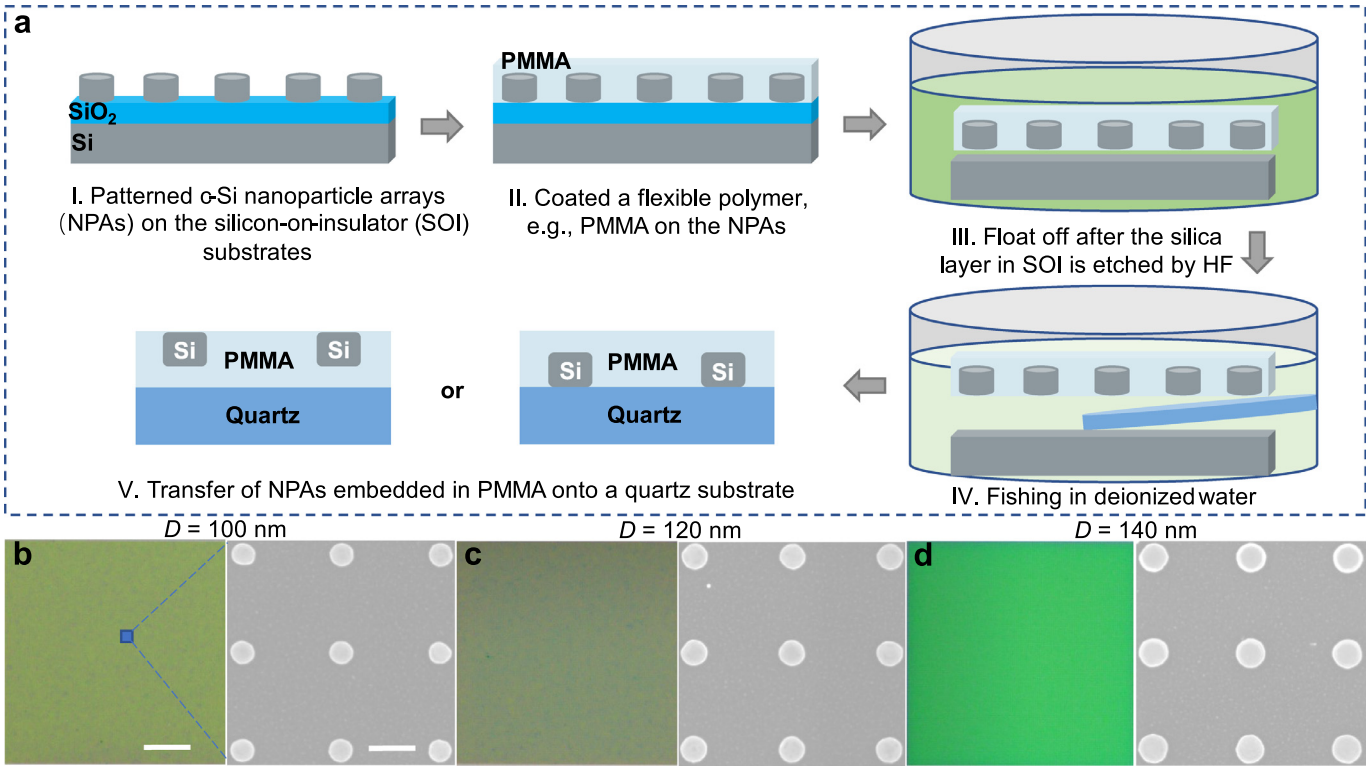

Fig. 2. Schematic of the fabrication processes. (a) The c-Si NPAs are prepared first on a silicon-on-insulator (SOI) wafer (see the details in Fig. S2). The bright-field microscope images of the NPAs with D = 100, 120, and 140 nm after this process (process I) are shown at the left panels of **(b-d)**. The right panels of **(b-d)** correspond to the scanning electron microscope (SEM) images. The scale bars of optical and SEM images are 10 μm and 200 nm, respectively. After steps II to V in panel a, two types of samples are obtained, including the NPAs embedded in PMMA facing to the air or sticking on quartz. Their microscope images are shown in the left and right panels of Fig. 4a, respectively.

3.2. c-Si nanoparticle arrays on quartz

To investigate the optical response of c-Si NPAs, we developed a versatile method (Fig. 2a) to fabricate a flexible device and transfer it onto a quartz substrate. The c-Si film is available from commercial wafers of silicon on insulator (SOI) or sapphire. While both slides are not qualified for achieving high Q-resonators according to the opaque thick Si substrates or high refractive index of sapphire ($n \sim 1.8$). A wafer-bonding technique has been demonstrated to transfer the c-Si film from the SOI substrate onto quartz [35–37]. Instead of using expensive bonding equipment and complicated processes of stripping, we reverse the roadmap of processes to prepare the Si cylinder arrays on SOI in advance. The bright-field microscope images of the NPAs with a fixed height of H = 100 nm and varying diameters of D = 100, 120, and 140 nm are shown in the left panels of Fig. 2b-d, respectively. The unitary color of the samples qualitatively indicates the homogeneity of the nanoparticles and the reproducible pitch of the arrays, which are further confirmed by the scanning electron microscope images (see the right panels of Fig. 2b-d). Afterward, we transfer the samples onto quartz by a "float off" technique (Fig. 2a). We can successfully deposit the c-Si NPAs in terms of either sticking on quartz or facing the air (Fig. 4a) by flipping over the ~ 500 nm thick PMMA slide in water [44].

3.3. Evaluations of Mie SLRs

Next, we focus on the optical characterization of the samples. To elucidate the properties of bare SLRs, we covered the sample with a 200 μm thick superstrate of PDMS to obtain a nearly homogeneous dielectric environment for the NPAs, depicted schematically in the inset of Fig. 3a. At first, we analyze the extinction spectra of NPAs measured under the condition of normal incidence. Two pronounced peaks are observed in the extinction spectra of NPAs with the diameter of D = 100 nm and the period varying in the range P = 405 to 425 nm (Fig. 3a). The resonance wavelengths of these two peaks red shift linearly as a function of period, following almost the same trend (Fig. 3e). The long-wavelength sharp peaks with a pronounced extinction (~ 0.6) show a Q-factor of ~ 350 estimated by a Lorentzian fitting. This value is a factor of ~ 3 larger compared with that of poly-Si NPAs in Ref. [43].

When the diameter of the cylinders increases from D = 100 to 130 nm, the resonances at the short wavelength band do not shift. The resonance wavelength of this band is tuned by the period of the array and can be calculated by $\lambda_{RAs} = n_{eff}P$, where n_{eff} is the effective index defining the phase velocity of the RAs. The slope of the curve representing the change of the resonance wavelength of the RAs as a function of period, shown as open circles in panels e and f of Fig. 3, determines the value of n_{eff} = 1.43.

The extinction increases due to the enhanced polarizability and scattering cross-section of Mie resonances as D becomes larger (Fig. S3). Besides the RA band of D = 130 nm, we observe two pronounced peaks in Fig. 3b. One of which is sharp with $Q \sim 400$ (indicated by downward orange triangles in Fig. 3f) and another relative broad with $Q \sim 80$ (indicated by upward orange triangles in Fig. 3f). We denote the resonance wavelengths of these two peaks by black upward and downward triangles in Fig. 3f, respectively. Both resonances red shift linearly following the same trend of RAs as P increases, manifesting the remarkable characteristics of SLRs. [55]

We have performed FDTD simulations to attribute the electromagnetic multipoles corresponding to the SLR peaks in the spectra. We simulated the extinction spectra (Fig. S4), which are qualitatively in agreement with the measurements, and the distribution of electric field intensity in a unit cell of the c-Si NPAs (panels c and d of Fig. 3) under

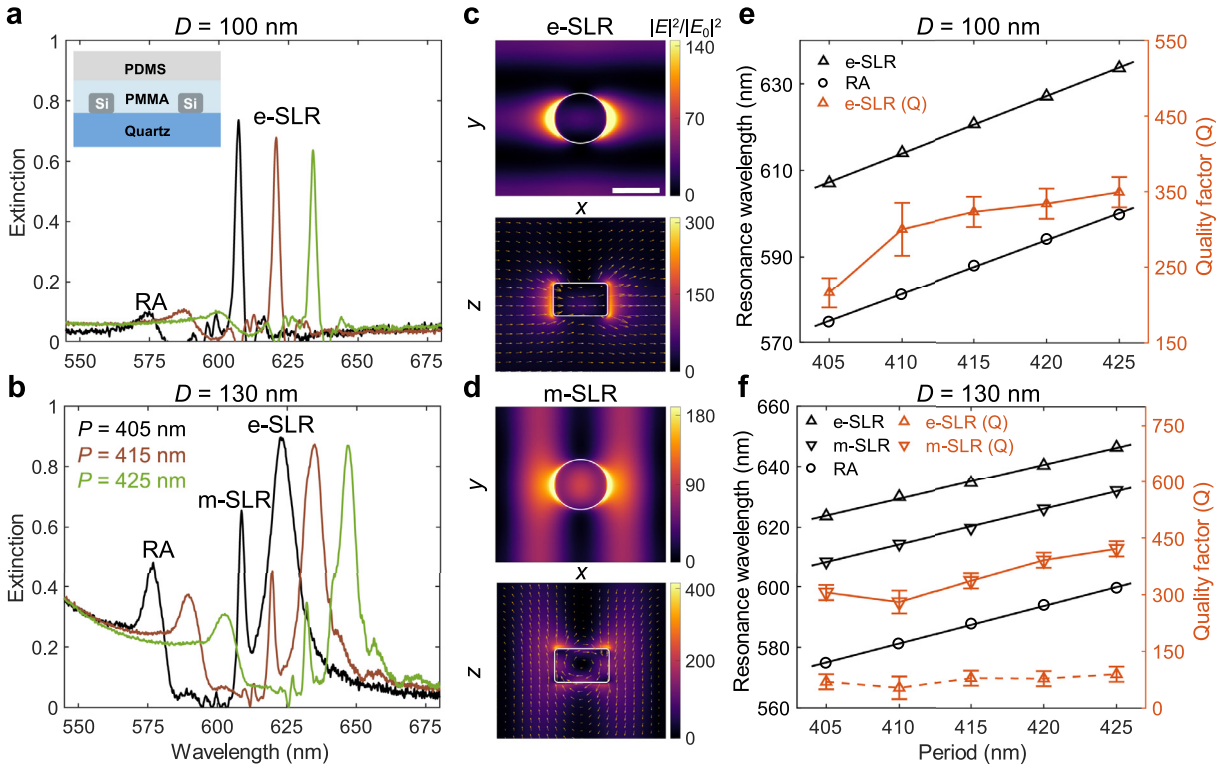

Fig. 3. SLRs in c-Si NPAs surrounded by a nearly homogeneous medium. (a) (b) Extinction spectra of the sample at normal incidence. The inset of panel a shows the schematic cross-section view of the sample covered with a PDMS superstrate ($n = 1.43$). The diameters of the nanoparticles corresponding to panels a and b are $D = 100$ and 130 nm, respectively. The black, brown, and green solid curves represent the spectra of the array with $P = 405$, 415, and 425 nm, respectively. **(c) (d)** FDTD simulations of the spatial distribution of the electric field intensity $|E|^2$ normalized to the incident field intensity $|E_0|^2$ in xy- and xz-planes of a unit cell of the array with $P = 405$ nm and $D = 130$ nm. The resonance wavelengths in panels c and d correspond to e-SLR ($\lambda = 625$ nm) and m-SLR ($\lambda = 608$ nm) indicated in panel b, respectively. The color scale represents the electric field enhancements and the yellow arrows are the real components of the electric vector field projected in xy or xz-planes. The contours of the nanoparticles are indicated by white circles and rectangles. Scale bar: 150 nm. **(e) (f)** The evolution of resonance wavelengths and Q-factors as a function of P, calculated from the extinction spectra shown in panels a and b. The resonance wavelengths of e-SLRs (black upward triangles) and m-SLRs (black downward triangles) red shift linearly with P, which follows the dependence of RAs (black circles). The Q-factors of SLRs (denoted by the orange triangles with error bars) increase as the resonances redshift.

the normal incidence of in-plane waves. For $P = 405$ nm, the peaks at $\lambda = 608$ nm in Fig. 3a and $\lambda = 623$ nm in Fig. 3b display the same field distribution as shown in Fig. 3c. From the cross-section (xz-plane) of the particle, the electric field is aligned with the polarization of the incident field and the intensity shows a dipolar field pattern. The top view (xy-plane) indicates that the radiative coupling between the particles is along the y-axis, thus perpendicular to the polarization of the incident field. The near-field distribution suggests that the peaks with the highest extinction shown in panels a and b of Fig. 3 arise from the collective coupling of electric Mie dipoles in the particles, and we label this resonance as e-SLR. In Fig. 3d, a loop of the electric field inside the particle in xz-plane manifests a magnetic dipole along the y-axis determined by the curl of the electric field. We further confirm from the xy-plane at the surface of the NPAs that the radiative coupling is along the x-axis, which is perpendicular to the magnetic dipole. The middle peaks in the spectra depicted in Fig. 3b correspond to the collective coupling of magnetic dipoles in the particles, and we label this resonance as m-SLR. We also compared the resonances of c-Si and a-Si NPAs by simulations (see the results in panels a and b of Fig. S4). The Q-factors of resonances in a-Si NPAs are much lower and especially the m-SLRs are not visible, compared with those of c-Si NPAs.

We have thus obtained an unambiguous and stronger m-SLR than previous measurements with poly-Si due to the strong field distribution inside particles and the negligible material losses of c-Si at wavelengths longer than 600 nm [43]. The c-Si NPAs offer a superior platform for achieving strong optically induced magnetic resonances of nonmagnetic structured elements. We also note that the fields of e-SLR and m-SLR display an extremely strong intensity enhancement, compared to the local field of Mie resonances near the isolated particles (Fig. S3).

The high Q-factor and collective behavior of Mie resonances upon excitation of SLRs within c-Si NPAs could enhance the ensemble coupling of quantum emitters, such as dye molecules or excitons in 2D semiconductors, at the proximity of the particles [5,45,56]. For molecules, we can easily disperse them homogeneously around the particles. However, to couple with 2D semiconductors requires an architecture with flat morphology to preserve their intrinsic optical properties [57]. Considering this application, we fabricated a c-Si NPAs facing air with a nearly planarized surface (roughness: 3.3 ± 0.7 nm depicted in Fig. S2). The schematic and optical microscope images of the sample, and a similar one with the NPAs in contact with the substrate, are shown in the left and right panels of Fig. 4a, respectively. Both NPAs are embedded in a PMMA layer with a thickness of ~ 530 nm, while without PDMS superstrate covering on top in this case. The structures of the two samples are mirror-symmetric due to the flipping process during the fabrication process of wet-transfer. At first glance, the color displays a pronounced difference by only changing the dielectric environments for the NPAs from air to quartz ($n = 1.45$). Panels b and c in Fig. 4 compare the extinction spectra of two samples with diameters $D = 100$ and 130 nm at normal incidence, respectively. The dash-dotted and solid curves represent the extinction spectra of NPAs facing the air (Si/air) and sticking on the quartz (Si/quartz), respectively. The resonances as a function of the period are consistent with the results shown in Fig. 3. We still pay

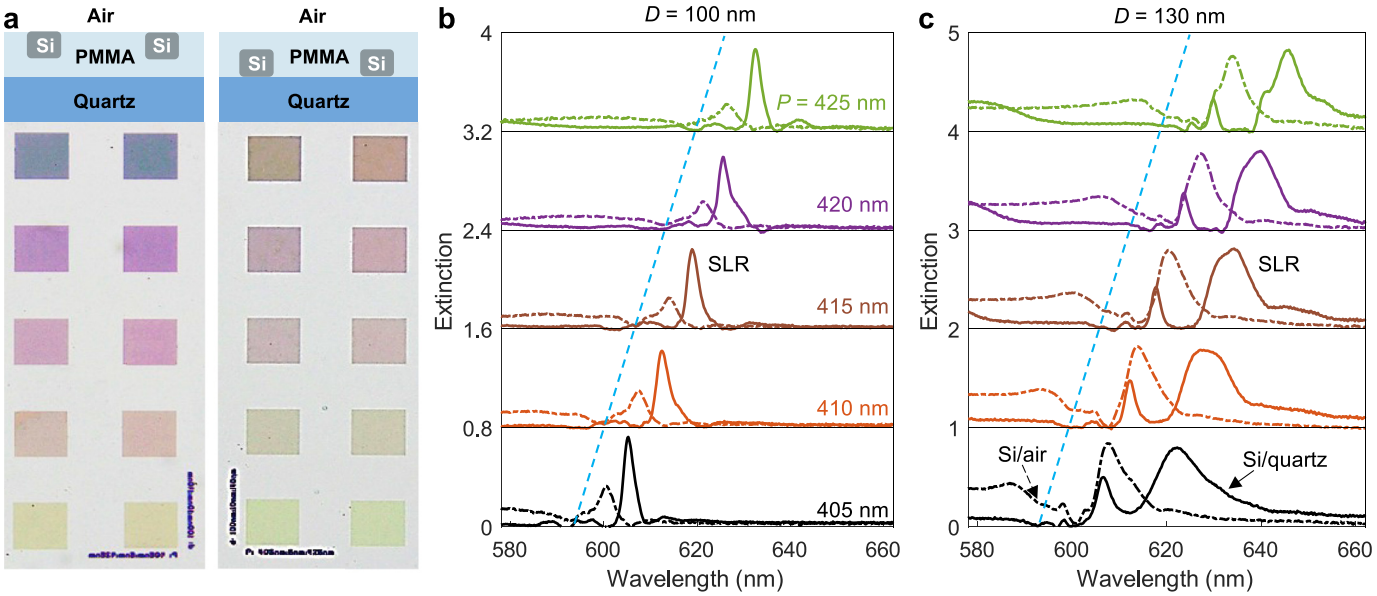

Fig. 4. SLRs in the c-Si NPAs embedded in a polymer slab. (a) Schematics of two samples showing the cross-section view and their corresponding bright-field microscope images from the top view. Scale bar: 50 μm. The samples on the left correspond to the c-Si nanoparticles facing air (labeled as Si/air) and the ones on the right to the nanoparticles directly on top of quartz (Si/quartz). The thickness of the PMMA layer is ~ 530 nm. The geometry parameters of the NPAs at the left and right columns of the two samples are mirror-symmetric, while their colors show pronounced differences. The nanoparticles in every column are of the same diameter. The period of the arrays from the bottom to top row varies from P = 405 to 425 nm. **(b) (c)** Corresponding extinction spectra of the NPAs at normal incidence with D = 100 and 130 nm, respectively. The dash-dotted and solid curves represent the spectra of the samples shown on the left and right panels of a, respectively. The oblique dashed lines denote the shift of SLRs as the period of the array changes.

attention to the pronounced peaks of SLR at longer wavelengths than the oblique-dashed line in panels b and c of Fig. 4. The increase of effective index for the RAs from the case of Si/air to that of Si/quartz gives rise to the red-shift of the SLRs. Such variation turns more significant for the NPA with a larger diameter of particles. Moreover, the m-SLRs have stronger and sharper peaks for D = 130 nm due to the enhanced radiative coupling between nanoparticles embedded in a nearly homogeneous dielectric environment (here is PMMA/Si/quartz). The spectral characterization confirms the successful fabrication of planarized NPAs with a flat surface, providing us a desirable platform to integrate 2D materials on top.[44,56]

3.4. Determination of BIC resonances

We have identified different SLRs from the extinction spectra at normal incidence and their near-field distributions. In this way, we could have missed sub-radiant collective resonances or dark modes, e.g. out-of-plane electric or magnetic dipoles and quadrupoles. To obtain the full dispersion information of our samples, we further investigate the wave-vector dependence extinction spectra by Fourier imaging and multipole decomposition. Panels a and c in Fig. 5 show the extinction dispersions of the NPAs with a fixed period of P = 405 nm and different diameters of D = 130 and 140 nm, respectively. We plot other data associated with different diameters in Fig. S6. Note that the measured NPAs are embedded in a thinner PMMA with a thickness of ~ 390 nm. The dispersions of NPAs are analyzed under TE polarization herein.

Around the wavelength of 600 nm, the wave-vector dependence of SLRs for a small nanoparticle diameter (D = 100 nm) follows the expected dispersion of a coupled oscillator model by mixing RAs and Mie resonances in individual nanoparticles (see Fig. S6a) [43,55]. The TE polarization modes show linear and parabolic dispersion curves simultaneously, associated with the e-SLRs and m-SLRs, which is consistent with the previous study in Ref.[43]. By increasing D (panels a-e in Fig. S6), the parabolic band gradually turns to a double band, and the linear dispersion bands split at the degenerated Γ point. Such pronounced variations of the energy bands are due to the strong coupling between the multipoles inside the nanoparticle with large diameters. For $D \geq$ 130 nm, we highlight two "dark" mode regions by dashed-white circles in panels a and c of Fig. 5 and panel a of Fig. S7 which are observable with nearly zero extinction at $k_{\parallel}/k_0 = 0$.

To clarify the "dark" modes, we cut through the dispersion curves and plot the extinction spectra as a function of incident wave vectors in panels e and g of Fig. 5 corresponding to the spectra of D = 130 and 140 nm, respectively. The variations of the two extinction peaks corresponding to the two "dark" modes are marked by the dashed-blue guides to the eye curves. Due to the mirror symmetry of the dispersion curves, we only evaluate the optical bands with positive wave-vectors from $k_{\parallel}/k_0$ = 0.05 to 0.2. We notice as well that the extinctions of the "dark" modes of D = 130 nm at $k_{\parallel}/k_0 = 0$, labeled by blue arrows in panel e of Fig. 5, still display a kink with certain visibility of extinction. In addition, the resonance at 600 nm for D = 140 nm does not behave fully dark as well, while the real dark mode appears at λ = 660 nm at $k_{\parallel}/k_0 = 0$ for the same NPA. We further calculate the Q-factors of the extinction peaks, indicated by the right dashed-blue curves in panels e and g, which are summarized in panels f and h of Fig. 5. The Q-factors for NPAs with D = 130 and 140 nm both increase as $k_{\parallel}/k_0$ is close to 0, implying that the Q-factors of the real dark modes in D = 140 nm should be larger than a readable value of $Q \sim 180$ at $k_{\parallel}/k_0$ = 0.05. The extinction turns dark and the Q-factors of the resonances rise as the bands are close to Γ point due to the suppression of radiation losses, manifesting the resonance at 660 nm for the NPA with D = 140 nm as a symmetry-protected BIC and at 595 nm as a quasi-BIC [54].

To elucidate the origin of the BIC mode, we focus on investigating the NPA with D = 140 nm. We employ the multipole decomposition approach to attribute the optical bands observed from the dispersion measurement. We record the field amplitude inside the nanoparticle for a unit cell of the array accompanied by the simulation of its extinction dispersion. We further calculate the scattering cross-section of each multipole induced from the electron/magnetic dipolar and quadrupolar moments. The simulated dispersion bands shown in panels b and d of

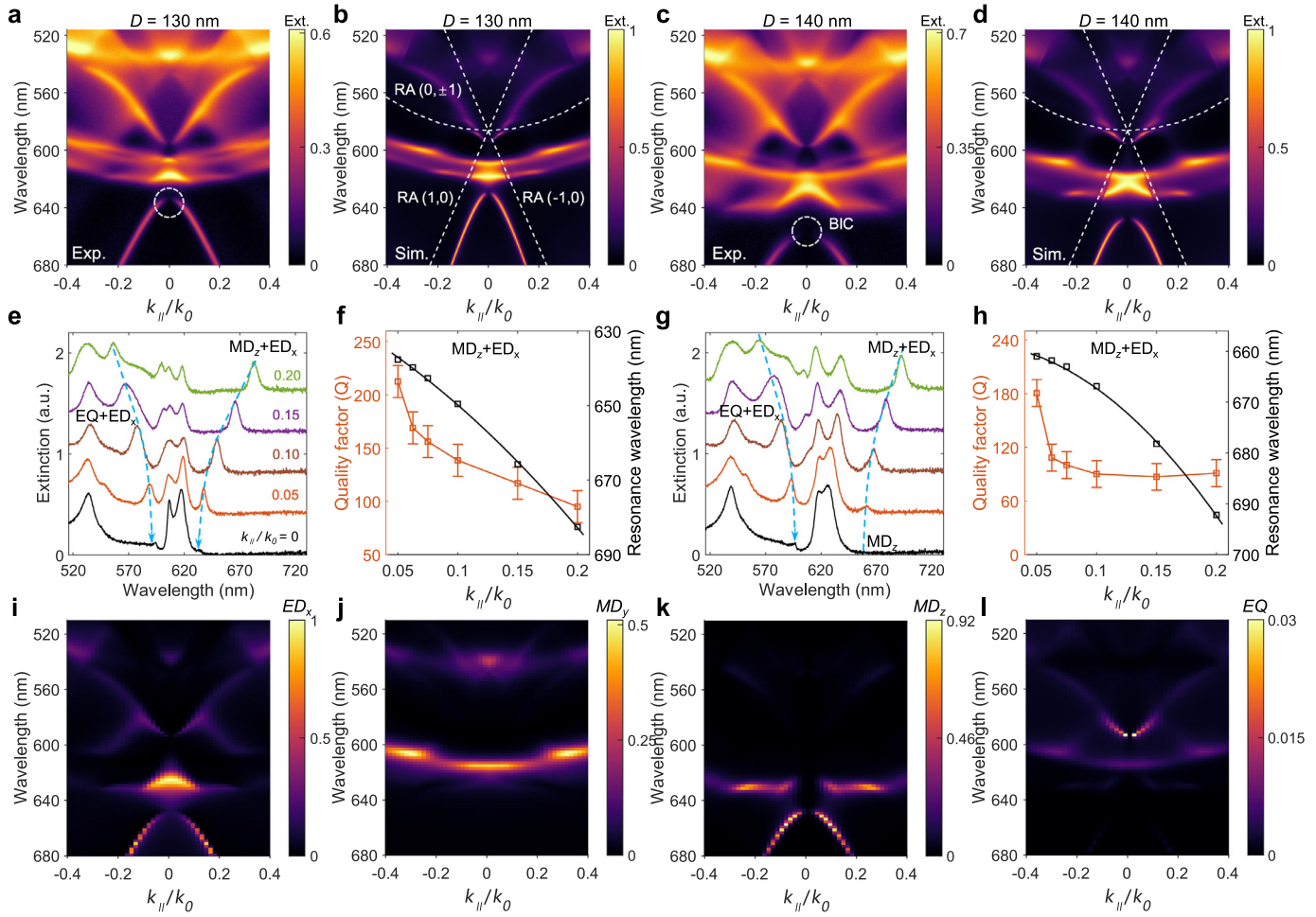

Fig. 5. Identifying symmetry-protected BICs from the extinction dispersion. (a) (c) Measured dispersion curves by Fourier imaging of the NPAs schematically depicted in Fig. S5, with D =130 and 140 nm while P = 405 nm for TE-polarized light. The NPAs are coated with a PMMA layer with a thickness of 390 nm. **(b) (d)** Simulated dispersion curves of NPAs by FDTD. The white linear and parabolic dashed curves represent the dispersion of RA (1, 0), (-1, 0), and RA (0, ± 1), respectively, calculated by the first order of the grating equation. **(e) (g)** Extinction spectra as a function of the wave vector of incident beam obtained by cutting through the dispersion curves in panels a and c. The dashed-blue curves are guides to the eye for the evolution of in-plane electric quadrupole (EQ) plus electric dipole (ED_x), and the out-of-plane magnetic dipolar (MD_z) plus electric dipole (ED_x) modes identified from the multipole decomposition depicted in panels i-l. The arrow denotes the kick on the extinction curves at $k_{\|}/k_0 = 0$, manifesting the properties of a quasi-BIC. **(f) (h)** Analysis of the Q-factors and resonance wavelength as a function of the incident wave-vector around BIC modes, denoted by dashed-white circles in panels a and c, which represent the MD$M\,D_z$ modes. Normalized-scattering cross-sections of multipoles in the NPA with the same parameters shown in panels c and d calculated by the approach of multipole decomposition, including ED_x **(i)**, in-plane magnetic dipole (MD_y) **(j)**, MD_z **(k)**, and EQ **(l)**.

Fig. 5 have a good agreement with the measurement, although the extinction at wavelengths below 600 nm is much lower than that of the measurements. This discrepancy could be due to a difference in the index of refraction between the c-Si film employed in the simulation and the real nanoparticles after fabrication. Panels i-l in Fig. 5 show that the dispersion of the scattering cross-section of the NPA is dominated by the optically induced in-plane electric dipoles (ED_x) and magnetic dipoles (MD_y), out-of-plane magnetic dipoles (MD_z), and in-plane electric quadrupoles (EQ), respectively. The scattering cross-section of the EQ is one order of magnitude lower than those of the other three multipoles due to the low probability to excite the EQ from the far field.

The pronounced extinction bands in Fig. 5d are the convolution of different multipoles. We compare the scattering spectra of $k_{\|}/k_0 = 0$ and $k_{\|}/k_0 = 0.05$ as an example, which is depicted in Fig. S8. At $k_{\|}/k_0 = 0$, there are two scattering peaks distinguishable with ED_x and MD_y. While the two dark bands at 588 and 650 nm with zero scattering at $k_{\|}/k_0 = 0$ rise up at $k_{\|}/k_0 = 0.05$. The former is dominated by the scattering from ED_x and EQ, and the latter is contributed by ED_x and MD_z. Therefore, we label the left dashed-blue bands (in the panels e and g of Fig. 5) as $EQ + ED_x$ and the right one as $MD_z + ED_x$. In other words, the occurrence of EQ and MD_z only at the condition of higher wave vectors implies that the dark modes corresponding to the observed quasi-BIC at the higher energy band (λ = 595 nm) and the BIC with lower energies (λ = 660 nm) in experiments arise from the in-plane quadrupole and out-of-plane magnetic dipoles, respectively. The measured quasi-BIC with not fully dark extinction at $k_{\|}/k_0 = 0$ could be due to the radiation channels to the diffraction orders of the lattice (indicated by the dashed-white curves in Fig. 5d).

3.5. Revealing QGMs at short-wavelength band

We have investigated collective resonances at wavelengths longer than 600 nm, in the range of which the absorption coefficient of c-Si is negligible. In the dispersion curves presented in panels a-e of Fig. S6, we can also observe the arising of a sharp resonant band around $\lambda = 530$ nm, which redshifts as the diameter of nanoparticles increases. This sharp resonance disappears when we use a superstrate of PDMS on top of the NPAs embedded in PMMA (see the panels f-j in Fig. S6). For clarification,

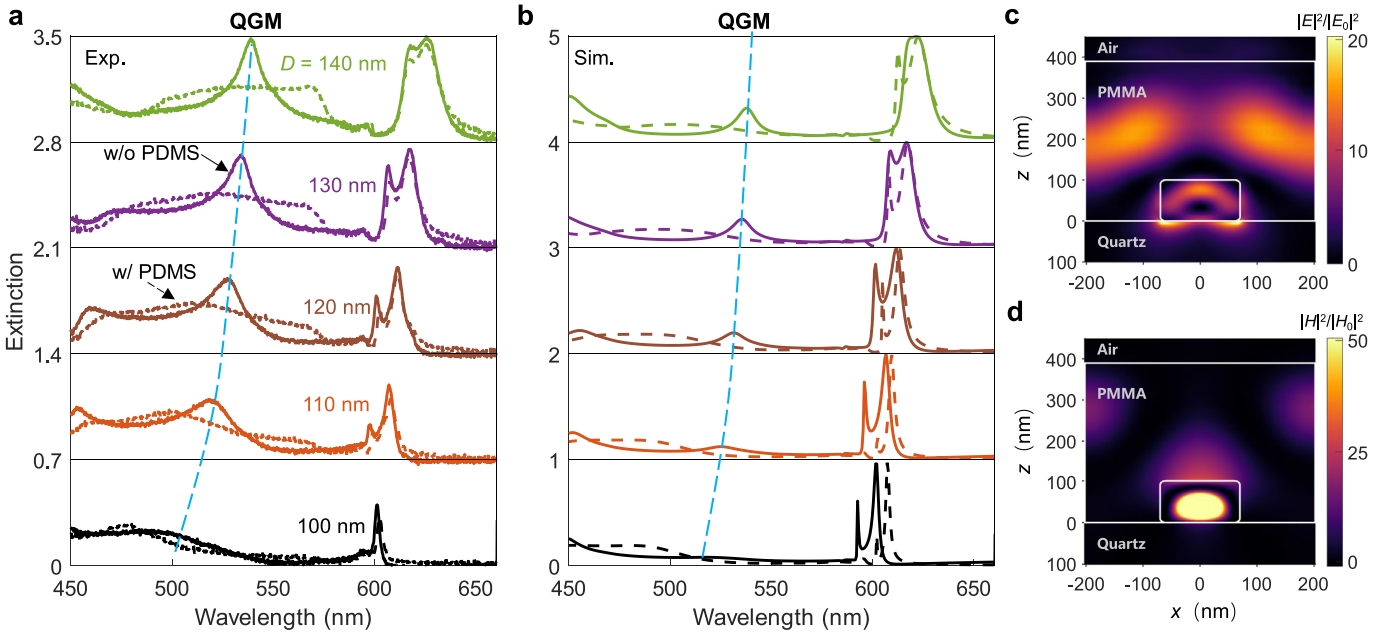

Fig. 6. QGMs at short wavelengths. (a) Comparison of the extinction spectra at normal incidence for the same sample with (dashed curves) or without (solid curves) a 200 μm thick PDMS superstrate. The schematics of the samples are shown in panels b and c of Fig. S5. The spectra are obtained by cutting through the corresponding dispersion curves in Fig. S6 at $k_{\parallel}/k_0 = 0$. The data corresponds to the NPAs with D in the range of 100 nm to 140 nm, from the bottom to the top. **(b)** Simulated spectra corresponding to panel a. The blue dashed curves in panels a and b are guides to the eye, identifying that the QGMs only occur in the NPAs embedded in the PMMA slab. FDTD simulations of electric **(c)** and magnetic **(d)** field distributions at xz-plane of a unit cell of the NPA with D = 140 nm. The resonance wavelength corresponds to QGM denoted in panel b.

we plot the extinction of NPAs with (dashed curves) or without (solid curves) the PDMS superstrate at $k_{\parallel}/k_0 = 0$ in Fig. 6a obtained by cutting through the corresponding Fourier images shown in Fig. S6. Comparing the spectra for the two cases, we see that the resonances almost overlap at longer wavelengths than 600 nm, while a peak protrudes above the Mie resonances with a broad spectrum at a shorter wavelength than 550 nm. The simulations follow the same trend as the experiment, denoted by the dashed blue curves in Fig. 6b.

The near-field distribution is simulated for the sharp resonances of the NPA embedded in the PMMA slab and $D = 140$ nm (panels c and d of Fig. 6). The strong field enhancement resembles a planar guided mode, which extends from the nanoparticles to the slab, with an anti-node at the center of the slab. Additionally, the decomposition results identify that the new sharp resonance is associated with the multipoles of ED_x and MD_y (panels i and j of Fig. 5). The hybridization of planar guide modes and multipole Mie resonances leads to a QGM [5,6,49]. Combining QGMs with SLRs or BICs, the c-Si NPAs embedded in PMMA can support two strong and high-Q resonances distributed in different optical windows, offering an efficient scheme for simultaneously enhancing the excitation and emission efficiency of quantum emitters in solid-state lighting devices [6].

4. Conclusion

In summary, we have demonstrated high-Q Mie resonances in the visible band from c-Si nanoantenna arrays. These collective resonances arise from the enhanced in-phase coupling between in-plane electric/magnetic dipoles and quadrupoles, or out-of-plane dipoles within the nanoantennas. Such collective coupling suppresses the radiation losses of the Mie resonances, which crucially limit the performance of isolated antennas. Thanks to the low absorption coefficients of c-Si, we have reduced the material losses of the nanoantenna arrays. We have also found that the quality of SLRs can be improved by decreasing the diameter of nanoparticles, while symmetry-protected BIC and QGMs only appear with a larger diameter of nanoparticles. We believe that the Q-factors of collective resonances can be further improved at short bands around 500 nm by optimizing the geometry parameters of the c-Si nanoantenna array, which will be our subsequent study. The abundant lattice resonances with high Q-factors and strong field enhancements inherent in c-Si NPAs could allow us many possibilities for investigating highly efficient and active light-emitting metasurfaces.

Declaration of competing interest

The authors declare that they have no conflicts of interest in this work.

Acknowledgements

We thank the technique support from Prof. Wen Qiao, Prof. Cheng Zhang, Liujing Li, Prof. Peng Li, and Prof. Wei Wang. We also thank the helpful discussion with Prof. Shunsuke Murai of the Kyoto University of Japan. This work was financially supported by the National Natural Science Foundation of China (62120106001, 62275184, 61875143, and 62104165), the Natural Science Foundation of Jiangsu Province (BK20200859, BK20200857, and BK20210713), and the Priority Academic Program Development (PAPD) of Jiangsu Higher Education Institutions. JGR and PB also acknowledge financial support from Nederlandse Organisatie voor Wetenschappelijk Onderzoek (NWO) (Vici 680-47-628).

Supplementary material

The Supplementary Materials include the pattern of the device layer of SOI wafer, measurement of the surface morphology of NPA, electromagnetic analysis of single nanoparticle, comparing the quality of c-Si and a-Si nanoantenna array by simulations, Extinction dispersion measured by μ-Fourier imaging, and Electromagnetic Multipole Decomposition.

Supplementary material associated with this article can be found, in the online version, at doi:10.1016/j.fmre.2022.05.020

References

[1] L. Novotny, N. Van Hulst, Antennas for light, Nat. Phot. 5 (2) (2011) 83–90.
[2] W. Wang, M. Ramezani, A.I. Väkeväinen, et al., The rich photonic world of plasmonic nanoparticle arrays, Mater. Today 21 (3) (2018) 303–314.
[3] F.J. Garcia-Vidal, C. Ciuti, T.W. Ebbesen, Manipulating matter by strong coupling to vacuum fields, Science 373 (6551) (2021) eabd0336.
[4] L. Tang, S.E. Kocabas, S. Latif, et al., Nanometre-scale germanium photodetector enhanced by a near-infrared dipole antenna, Nat. Photon. 2 (4) (2008) 226–229.
[5] S. Wang, Q. Le-Van, T. Peyronel, et al., Plasmonic nanoantenna arrays as efficient etendue reducers for optical detection, ACS Photon. 5 (6) (2018) 2478–2485.
[6] G. Lozano, D.J. Louwers, S.R. Rodríguez, et al., Plasmonics for solid-state lighting: enhanced excitation and directional emission of highly efficient light sources, Light Sci. Appl. 2 (5) (2013). e66–e66
[7] P.P. Iyer, R.A. DeCrescent, Y. Mohtashami, et al., Unidirectional luminescence from ingan/gan quantum-well metasurfaces, Nat. Photon. 14 (9) (2020) 543–548.
[8] M. Ramezani, A. Halpin, A.I. Fernández-Domínguez, et al., Plasmon-exciton-polariton lasing, Optica 4 (1) (2017) 31–37.
[9] S.T. Ha, Y.H. Fu, N.K. Emani, et al., Directional lasing in resonant semiconductor nanoantenna arrays, Nat. Nanotechnol. 13 (11) (2018) 1042–1047.
[10] M. Wu, S.T. Ha, S. Shendre, et al., Room-temperature lasing in colloidal nanoplatelets via mie-resonant bound states in the continuum, Nano Lett. 20 (8) (2020) 6005–6011.
[11] A.E. Cetin, A.F. Coskun, B.C. Galarreta, et al., Handheld high-throughput plasmonic biosensor using computational on-chip imaging, Light Sci. Appl. 3 (1) (2014). e122–e122
[12] M.L. Tseng, Y. Jahani, A. Leitis, et al., Dielectric metasurfaces enabling advanced optical biosensors, ACS Photon. 8 (1) (2020) 47–60.
[13] J.N. Farahani, D.W. Pohl, H.-J. Eisler, et al., Single quantum dot coupled to a scanning optical antenna: a tunable superemitter, Phys. Rev. Lett. 95 (1) (2005) 017402.
[14] Y. Chen, M. Zopf, R. Keil, et al., Highly-efficient extraction of entangled photons from quantum dots using a broadband optical antenna, Nat. Commun. 9 (1) (2018) 1–7.
[15] A.G. Curto, G. Volpe, T.H. Taminiau, et al., Unidirectional emission of a quantum dot coupled to a nanoantenna, Science 329 (5994) (2010) 930–933.
[16] R. Chikkaraddy, B. De Nijs, F. Benz, et al., Single-molecule strong coupling at room temperature in plasmonic nanocavities, Nature 535 (7610) (2016) 127–130.
[17] J.B. Pendry, A.J. Holden, D.J. Robbins, et al., Magnetism from conductors and enhanced nonlinear phenomena, IEEE Trans. Microwave Theory Tech. 47 (11) (1999) 2075–2084.
[18] A.I. Kuznetsov, A.E. Miroshnichenko, M.L. Brongersma, et al., Optically resonant dielectric nanostructures, Science 354 (2016) aag24721–8.
[19] I. Staude, A.E. Miroshnichenko, M. Decker, et al., Tailoring directional scattering through magnetic and electric resonances in subwavelength silicon nanodisks, ACS Nano 7 (9) (2013) 7824–7832.
[20] U. Zywietz, A.B. Evlyukhin, C. Reinhardt, et al., Laser printing of silicon nanoparticles with resonant optical electric and magnetic responses, Nat. Commun. 5 (1) (2014) 1–7.
[21] C. Wang, Z. Jia, K. Zhang, et al., Broadband optical scattering in coupled silicon nanocylinders, J. Appl. Phys. 115 (24) (2014) 244312.
[22] R.M. Bakker, D. Permyakov, Y.F. Yu, et al., Magnetic and electric hotspots with silicon nanodimers, Nano Lett. 15 (3) (2015) 2137–2142.
[23] A.E. Miroshnichenko, A.B. Evlyukhin, Y.F. Yu, et al., Nonradiating anapole modes in dielectric nanoparticles, Nat. Commun. 6 (1) (2015) 1–8.
[24] R. Regmi, J. Berthelot, P.M. Winkler, et al., All-dielectric silicon nanogap antennas to enhance the fluorescence of single molecules, Nano Lett. 16 (8) (2016) 5143–5151.
[25] A. Tittl, A. Leitis, M. Liu, et al., Imaging-based molecular barcoding with pixelated dielectric metasurfaces, Science 360 (6393) (2018) 1105–1109.
[26] S. Murai, D.R. Abujetas, G.W. Castellanos, et al., Bound states in the continuum in the visible emerging from out-of-plane magnetic dipoles, ACS Photon. 7 (8) (2020) 2204–2210.
[27] S.I. Azzam, K. Chaudhuri, A. Lagutchev, et al., Single and multi-mode directional lasing from arrays of dielectric nanoresonators, Laser Photon. Rev. 15 (3) (2021) 2000411.
[28] A.A. Bogdanov, K.L. Koshelev, P.V. Kapitanova, et al., Bound states in the continuum and fano resonances in the strong mode coupling regime, Adv. Photon. 1 (1) (2019) 016001.
[29] K. Koshelev, S. Kruk, E. Melik-Gaykazyan, et al., Subwavelength dielectric resonators for nonlinear nanophotonics, Science 367 (6475) (2020) 288–292.
[30] D.G. Baranov, D.A. Zuev, S.I. Lepeshov, et al., All-dielectric nanophotonics: the quest for better materials and fabrication techniques, Optica 4 (7) (2017) 814–825.
[31] W. Yang, S. Xiao, Q. Song, et al., All-dielectric metasurface for high-performance structural color, Nat. Commun. 11 (1) (2020) 1–8.
[32] J. Kühne, J. Wang, T. Weber, et al., Fabrication robustness in bic metasurfaces, Nanophotonics 10 (2021) 4373–4383.
[33] J. Wang, J. Kühne, T. Karamanos, et al., All-dielectric crescent metasurface sensor driven by bound states in the continuum, Adv. Funct. Mater. (2021) 2104652.
[34] E.D. Palik, Handbook of optical constants of solids, volume 3, Academic Press, 1998.
[35] D. Sell, J. Yang, et al., Visible light metasurfaces based on single-crystal silicon, ACS Photon. 3 (10) (2016) 1919–1925.
[36] Z. Zhou, J. Li, R. Su, et al., Efficient silicon metasurfaces for visible light, ACS Photon. 4 (3) (2017) 544–551.
[37] C. Zhang, Y. Xu, J. Liu, et al., Lighting up silicon nanoparticles with mie resonances, Nat. Commun. 9 (1) (2018) 1–7.
[38] T. Bucher, A. Vaskin, R. Mupparapu, et al., Tailoring photoluminescence from mos2 monolayers by mie-resonant metasurfaces, ACS Photon. 6 (4) (2019) 1002–1009.
[39] J. Hua, E. Hua, F. Zhou, et al., Foveated glasses-free 3d display with ultrawide field of view via a large-scale 2d-metagrating complex, Light Sci. Appl. 10 (1) (2021) 1–9.
[40] C. Zhang, K. Wu, V. Giannini, et al., Planar hot-electron photodetection with tamm plasmons, ACS Nano 11 (2) (2017) 1719–1727.
[41] C.H. Kang, I. Dursun, G. Liu, et al., High-speed colour-converting photodetector with all-inorganic cspbbr3 perovskite nanocrystals for ultraviolet light communication, Light Sci. Appl. 8 (1) (2019) 1–12.
[42] S. Murai, G.W. Castellanos, T. Raziman, et al., Enhanced light emission by magnetic and electric resonances in dielectric metasurfaces, Adv. Opt. Mater. 8 (16) (2020) 1902024.
[43] S. Wang, T. Raziman, S. Murai, et al., Collective mie exciton-polaritons in an atomically thin semiconductor, J. Phys. Chem. C 124 (35) (2020) 19196–19203.
[44] P. Liu, Z. Zhang, M. Lang, et al., Manipulating the directional emission of monolayer semiconductors by dielectric nanoantenna arrays, J. Optics 24 (2) (2022) 024005.
[45] S. Wang, S. Li, T. Chervy, et al., Coherent coupling of WS_2 monolayers with metallic photonic nanostructures at room temperature, Nano Lett. 16 (7) (2016) 4368–4374.
[46] E. Radescu, G. Vaman, Exact calculation of the angular momentum loss, recoil force, and radiation intensity for an arbitrary source in terms of electric, magnetic, and toroid multipoles, Phys. Rev. E 65 (4) (2002) 046609.
[47] R. Paniagua-Domínguez, Y.F. Yu, A.E. Miroshnichenko, et al., Generalized brewster effect in dielectric metasurfaces, Nat. Commun. 7 (1) (2016) 1–9.
[48] V.R. Tuz, A.B. Evlyukhin, Polarization-independent anapole response of a trimer-based dielectric metasurface, Nanophotonics 10 (2021) 4373–4383.
[49] G.W. Castellanos, P. Bai, J. Gómez Rivas, Lattice resonances in dielectric metasurfaces, J. Appl. Phys. 125 (21) (2019) 213105.
[50] V.G. Kravets, A.V. Kabashin, W.L. Barnes, et al., Plasmonic surface lattice resonances: A review of properties and applications, Chem. Rev. 118 (12) (2018) 5912–5951.
[51] A. Jain, A.R. James, J. Nogan, et al., Dark-state-based low-loss metasurfaces with simultaneous electric and magnetic resonant response, ACS Photon. 7 (1) (2020) 241–248.
[52] A.D. Utyushev, V.I. Zakomirnyi, I.L. Rasskazov, Collective lattice resonances: Plasmonics and beyond, Rev. Phys. 6 (2021) 100051.
[53] S. Murai, M.A. Verschuuren, G. Lozano, et al., Hybrid plasmonic-photonic modes in diffractive arrays of nanoparticles coupled to light-emitting optical waveguides, Opt. Express 21 (4) (2013) 4250–4262.
[54] K. Koshelev, S. Lepeshov, M. Liu, et al., Asymmetric metasurfaces with high-q resonances governed by bound states in the continuum, Phys. Rev. Lett. 121 (19) (2018) 193903.
[55] S. Wang, Q. Le-Van, F. Vaianella, et al., Limits to strong coupling of excitons in multilayer ws2 with collective plasmonic resonances, ACS Photon. 6 (2) (2019) 286–293.
[56] T. Chervy, S. Azzini, E. Lorchat, et al., Room temperature chiral coupling of valley excitons with spin-momentum locked surface plasmons, ACS Photon. 5 (4) (2018) 1281–1287.
[57] S. Eizagirre Barker, S. Wang, R.H. Godiksen, et al., Preserving the emission lifetime and efficiency of a monolayer semiconductor upon transfer, Adv. Opt. Mater. 7 (13) (2019) 1900351.

Zhenghe Zhang received his B.S. degree in Optoelectronic Information Science and Engineering from Hebei Normal University in 2020. He is currently a M.S. candidate at the School of Optoelectronic Science and Engineering at Soochow University. His current research interests are focused on the study of dielectric nanophotonics.

Xiaofeng Li received B.Eng. and Ph.D. degrees from Southwest Jiaotong University, China, in 2002 and 2007, respectively. From 2007 to 2011, he was working Nanyang Technological University (Singapore) and Imperial College London (U.K.), respectively. Since January 2012, he has been with Soochow University, Suzhou, China, as a Full Professor. He is now the Dean of School of Optoelectronic Science and Engineering as well as the vice president of Soochow University. He has published around 200 journal papers. His research interests are photovoltaics and photodetections.